NUMERICAL SIMULATION OF COMPRESSIBLE MIXING LAYERS

Arnab Chaudhuri[a], Abdellah Hadjadj[a] & Sandrine Palerm[b]
[a]CORIA - UMR, CNRS 6614, INSA de Rouen, Avenue de l'Université BP8, 76801 St Etienne du Rouvray, France
[b]CNES, Centre Spatial d'Evry, Rond-Point de l'Espace - 91023 Evry, France

ABSTRACT

A high-order, low dissipative WENO scheme together with a third-order Total Variation Diminishing (TVD) Runge-Kutta time stepping method have been utilized to examine the features of the turbulent mixing layers related to the nozzle flow application by Direct Numerical Simulation (DNS) study. The validation of a multi-species non-reacting parallel Navier-Stokes (NS) solver has been achieved through benchmark problems. A 2D shock/mixing-layer interaction has been solved prior to the DNS study of a temporal mixing layer for successful validation of the newly developed solver. The prediction of complex interactions between shocks (or shocklets) and vortices arising in supersonic-supersonic mixing layer and temporally evolving turbulent mixing layer with low convective Mach number (weakly compressible) are found in excellent agreement with the experimental and DNS results of literature.

INTODUCTION

Flow separation control in rocket nozzles is a challenging problem in aerospace science, not only for current engines confronted with problems of thermo-mechanical resistance, but also for the future engines which could operate with very wide separation zones and possible post combustion of the exhaust gases in the nozzle. These phenomena are related to a usually unstable and unsteady flow, occurring in large expansion nozzle leading to strong mechanical/ thermal loads, which are prejudicial to the mechanical structure of the nozzle. The mechanisms responsible for the thermal loads are still not well understood and only few studies are available in literature for nozzles with hot gas flow. The formation of mixing layers with possible post combustion near the end of the nozzle can be one of the main reasons for the wall heating and the so called "thermal end effect". Fig.1 depicts the formation of a mixing layer between the incoming fresh ambient air and the nozzle exit gas mixture streams along with the complex flow patterns inside the nozzle.

In order to understand the underlying fundamental physics of these phenomena, a DNS study is carried out for a non-reacting mixing layer in a sub-scale nozzle. Although substantial amount of investigations on the behavior of compressible mixing layers is available in the literature, the application of high-order numerical schemes with robust shock capturing abilities is not abundant. An in-house 3D explicit multi-species Navier-Stokes parallel MPI solver with variable physical and transport properties have been developed to simulate the formation of a compressible mixing layer utilizing Bandwidth Optimized fourth-order WENO (WENO-BWO) together with a total variation relative limiter [1]. A 2D supersonic-supersonic spatially evolving mixing layer, interacting with an impinging oblique shock has been solved as a benchmark problem. In this work, a DNS study is carried out further for non-reacting mixing layers keeping in view the transient nozzle-end characteristics. These computations can be used as a database for physical comprehension as well as for the validations of LES/DES models in real geometries. The results are compared and validated with DNS and experimental results available in literature. The present work is meant for the initial validation of the in-house multispecies NS solver by solving mixing layer problems associated to the end effects in the nozzle flow regime.

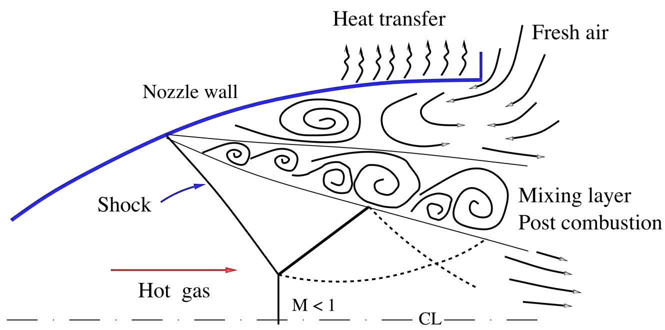

Fig.1. Schematic of overexpanded rocket nozzle with flow separation and mixing layer formation

NUMERICAL METHODOLOGY

The 3D unsteady compressible Navier-Stokes system of equations with multi-species transport equations excluding Dufour and Soret effects are solved. The thermally perfect gas behavior is assumed for each species so that the specific heats, enthalpy and the internal energy are functions of temperature only. The JANAF table is utilized to calculate these properties at a given temperature. The GRI-Mech [2] transport database is used to evaluate the viscosity coefficient, thermal conductivity and binary diffusion coefficient.

The efficient implementation of low-dissipative, high-order shock-capturing schemes is essential to avoid excessive damping of the flow features over a wide range of length scales as well as to nullify the spurious oscillations around shock waves and/or eddy shocklets. High-order WENO schemes [3] with local Lax-Friedrichs splitting for the calculation of numerical fluxes at cell interfaces have been utilized. The multi-species inviscid flux Jacobian **J** and its Eigen–value Eigen-vector decomposition $\mathbf{J} = \mathbf{R}^{-1}\, \Lambda\, \mathbf{R}$ are used to calculate the numerical fluxes at a cell interface. The developed code has been equipped with Bandwidth Optimized fourth-order WENO (WENO-BWO) utilizing a total variation relative limiter [1].

The diffusion terms are discretized using compact fourth-order central difference formulas [4]. A 3D parallel MPI flux-based finite difference solver has been developed using these schemes with the explicit third-order Runge-Kutta method for the time integration. In all the computations the CFL number has been taken as 0.7.

SHOCK MIXING LAYER INTERACTION

This benchmark problem of complex shock/mixing-layer interaction has been chosen to validate the WENO-BWO solver. An oblique shock wave is allowed to pass through the vortices arising from a spatially developing mixing layer, and numerical simulations are carried out to predict the complex shock-mixing layer interaction. The computational domain of normalized size L_x=200 and L_y=40 together with the other parameters for the configuration of this test case are taken similar to the ones presented by Yee et al. [5]. The ratio of specific heats γ =1.4, Reynolds number Re = 500 and Prandtl number Pr = 0.72 are utilized for all the simulations of this test case. Stream-1 (upper stream) and Stream-2 (lower stream) are associated to the left inflow boundary as mixing streams. The conditions for Stream-3 (entering through top boundary) are fixed from the flow properties behind an oblique shock with a wedge angle β=12°. The details of the flow parameters are given in Tab.1. A hyperbolic tangent profile of longitudinal velocity and perturbations in the transverse velocity (v=0) are added to the inflow as

$$u(\hat{y}) = 2.5 + 0.5\tanh(2\hat{y}) \tag{1}$$

$$v' = \sum_{k=1}^{2} a_k \cos(2\pi kt/T + \phi_k)\exp(-\hat{y}^2/b) \tag{2}$$

with $\hat{y} = y - L_y/2$, period $T = \lambda/u_c$, wave length $\lambda = 30$, $b = 10$, $a_1 = a_2 = 0.05\,\phi_1 = 0$ and $\phi_2 = \pi/2$. The convective Mach number $M_c = \dfrac{\Delta u}{c_1 + c_2}$ is 0.6, where $\Delta u = u_1 - u_2$.

Property	Stream-1	Stream-2	Stream-3
Longitudinal velocity, u	3.0000	2.0000	2.9709
Transverse velocity, v	0.0000	0.0000	-0.1367
Density, ρ	1.6374	0.3626	2.1101
Pressure, p	0.3327	0.3327	0.4754
Mach number	5.6250	1.7647	5.2956

Tab.1. Normalized flow properties of shock-mixing layer interaction problem

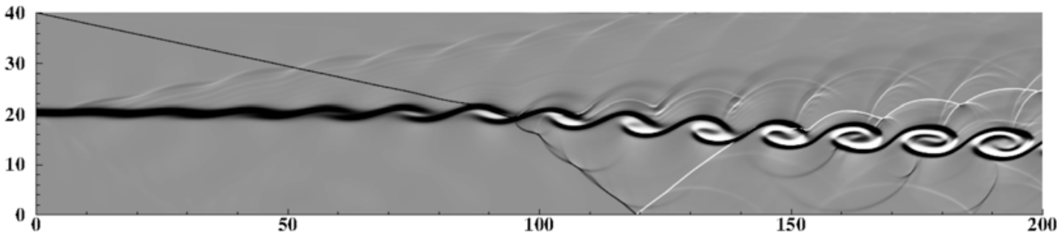

(a)

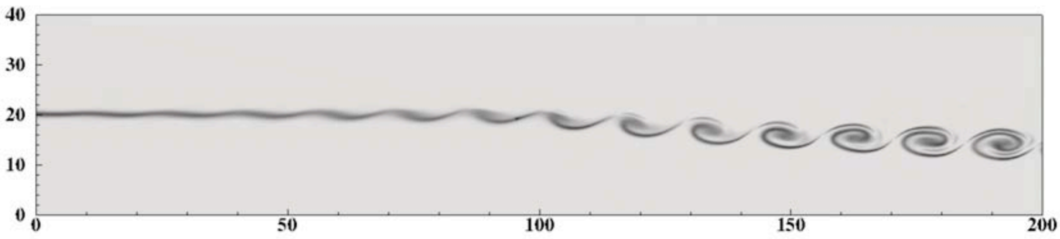

(b)

Fig. 2 (a) Numerical schlieren picture and (b) vorticity contour, of the shock/mixing layer interaction

Supersonic inflow (top and left boundary) and supersonic outflow (right boundary) conditions are implemented. However, at the bottom boundary, slip wall conditions are fixed to avoid any boundary layer formation and the possible complexity arising from the shock/ boundary layer interaction. A grid dependency study with the WENO-BWO scheme has been carried out taking 1024×256, 2048×512 and 4096×1024 mesh points. No substantial difference has been observed between the results of 2048×512 and 4096×1024 grids. It can be seen from the numerical schlieren based on density gradient (Fig.2a) that, at t = 120, the incident shock get refracted after interacting with the mixing layer (at x ≈ 90) followed by the reflection from the bottom slip wall. The attenuated reflected shock then penetrates through the developed vortices of the mixing zone. The passage of the reflected shock from the bottom boundary, penetrating through the vortex at x ≈149 is also visible in this figure. These findings are in excellent agreement with the results reported in [5]. The vorticity contour has been illustrated in Fig.2b. It can be realized that the locus of the center of the vortex cores is shifted below, towards the low-density side. This arises due to the momentum balance for mixing layers having density ratio other than unity. The vortex cores are associated to pressure wells and adjacent stagnation zones between two vortices are residing in pressure hills. The eddy-shocklets emanating from the circumference of the vortices in this region (150< x ≤ 200) and the secondary interactions among the neighboring shocks and vortices are also well captured by the simulation.

The mean flow-field have been extracted by time averaging over the period of t = 120 to 240. An approximate measure of the evolution of the mixing layer thickness has been shown in Fig.3, extracted from the mean longitudinal velocity. The mixing layer thickness δ(x) is defined as the distance where the mean longitudinal velocity satisfies $\langle u(x,y)\rangle \in \left[1.1\langle u(x,0)\rangle, 0.9\langle u(x,L_y)\rangle\right]$. It can be seen that the interaction of the reflected shock waves with the mixing zones has been manifested in the spatial evolution of the mixing layer thickness. The evolution of the mixing layer can be broadly classified into three zones, as shown in Fig.3 together with the linear curve fits. The first zone consists of a usual growth of the mixing layer there exists an increase in growth of mixing layer thickness after the first interaction with the oblique shock wave in the second zone. It is then followed by a saturated growth rate after the second interaction with the reflected shock wave.

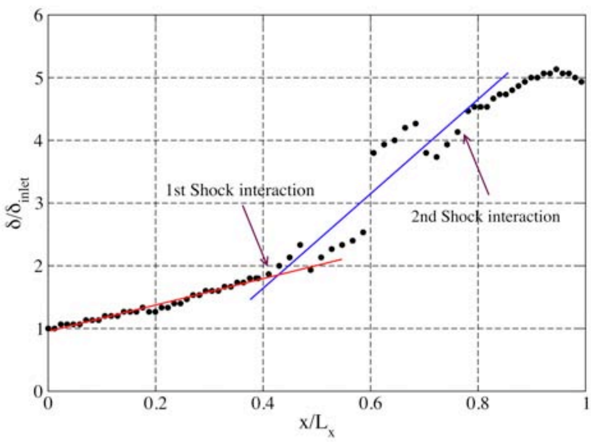

Fig. 3. Spatial evolution of mixing layer thickness

DNS OF TEMPORAL MIXING LAYER

Fig.4 shows the configuration of the temporally evolving mixing layer for the DNS study utilizing the WENO-BWO scheme. The DNS study has been carried out for a low convective Mach number (M_c= 0.1) test case with negligible compressibility effects. This test case can be considered as weakly compressible to compare with the experimental results of an incompressible shear layer. The two streams (O_2) are having the same initial pressure field (P_1= P_2= 10^5 Pa). The initial free stream temperature of the upper stream is 600K. Velocity and density fields are initialized by a hyperbolic tangent profile as given below

$$u(y) = \frac{\Delta u}{2} \tanh\left(\frac{y}{2\delta_{\theta,0}}\right) \tag{3}$$

$$\rho(y) = \rho_{ref}\left[1 + \lambda(s)\tanh\left(\frac{y}{2\delta_{\theta,0}}\right)\right] \tag{4}$$

with $s = \rho_1/\rho_2$ and $\lambda(s) = (s-1)/(s+1)$, the reference state being the arithmetic mean of state 1 and state 2. The initial temperature field profile is fixed similarly to that of the density field. The initial momentum thickness Reynolds number is $\mathrm{Re}_{\theta,0} = \frac{\delta_{\theta,0}\Delta u \rho_{ref}}{\mu_{ref}} = 160$. The initial vorticity thickness $\delta_{\omega,0}$ is equal to $4\delta_{\theta,0}$ and $\mathrm{Re}_{\omega,0} = 640$. The size of the computational domain normalized by the initial momentum thickness ($L_x \times L_x \times L_x$ = 345 × 172 × 86), and the number of mesh points (512 × 256 × 128) are taken similar to those reported in [6]. The computed integral lengths (l_x , l_z) and Kolmogorov scale (L_η) are found to be sufficiently small compared to the computational domain and the grid resolution is adequate to resolve both large and small scales of turbulence. The parallel NS solver used up-to 512 processors with 12,300 CPU hours per flow case.

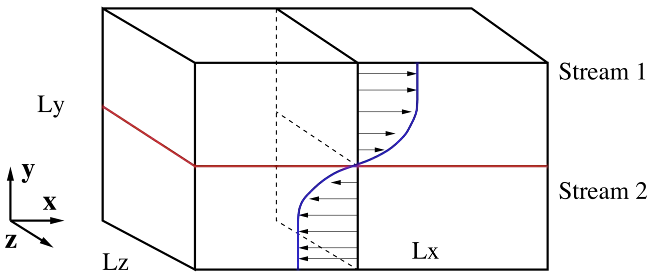

Fig.4 Schematic of temporal mixing layer

Flow Initialization

The initial turbulent fluctuations are added to the velocity field using a digital filter technique [7]. This procedure utilizes the prescribed Reynolds stress tensor and the length scales of the problem concerned to generate the corresponding fluctuating velocity field (inflow/initial), taking into account the nature of the autocorrelation function for the prevailing turbulence. The length scales are chosen as $\delta_{w,0}$ in each direction. The Reynolds stress tensor is assumed to have a Gaussian shape with amplitudes taken similar to the experimental peak intensities available for incompressible mixing layer flow in [8] as presented in [6] ($\sqrt{R_{11}}/\Delta u$ =0.193, $\sqrt{R_{22}}/\Delta u$ = 0.128, $\sqrt{R_{33}}/\Delta u$ =0.131, $\sqrt{R_{12}}/\Delta u$ = 0.117, $\sqrt{R_{13}}/\Delta u$ and $\sqrt{R_{23}}/\Delta u$ are assumed 0.1. The periodic boundary conditions are applied in x and z directions, while the slip condition has been applied in top and bottom boundaries (y direction).

Instantaneous structure and characteristics of the mixing layer

The computation is carried out up-to the non-dimensional time $\tau = t\Delta u/\delta_{\theta,0} = 820$, where the momentum thickness is defined as, $\delta_\theta = \frac{1}{\rho_{ref}\Delta u^2}\int_{-\infty}^{\infty}\bar{\rho}\left(\frac{1}{4}\Delta u^2 - \tilde{u}^2\right)dy$.

The Reynolds averaged $\bar{\phi}$ and Favre averaged $\tilde{\phi}$ quantities are space averaged quantities in the homogeneous directions (x and z). Fig.5 shows the evolution of the momentum thickness in time together with the DNS results of [6] for various convective Mach numbers. It can be seen that there exists linearity in the growth of the momentum thickness for $\tau > 500$.

The growth rate ($\dot{\delta}_\theta = \frac{1}{\Delta u}\frac{d\delta_\theta}{dt}$) for this case (slope of the linear curve fit) is found to be 0.016. The ratio of the vorticity and momentum thicknesses $D_\omega = \delta_\omega/\delta_\theta$ lies between 4 and 5 with $\mathrm{Re}_\omega = 9676$ at $\tau_{\max}$. This is in excellent agreement of the DNS growth rate of the quasi-incompressible case with M_c=0.3 of [6]. The iso-surfaces of invariant of the velocity gradient tensor, Q, defined by $Q = \left(\Omega_{ij}\Omega_{ij} - S_{ij}S_{ij}\right)/2$, where $S_{ij} = \left(u_{i,j} + u_{j,i}\right)/2$, $\Omega_{ij} = \left(u_{i,j} - u_{j,i}\right)/2$, is plotted for the flow visualization of the mixing layer. It is evident that the positive values of Q represent the vortex dominated flow. 3D perspective views of iso-surfaces of Q are presented in Fig.6 in self-similar state. The 3D complex vortex tubes structures are clearly evident from this figure.

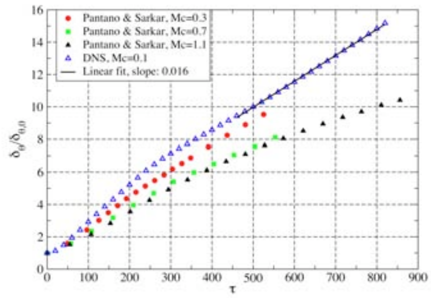

Fig.5. Evolution of momentum thickness

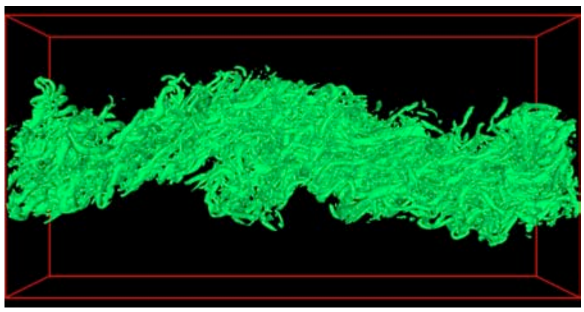

Fig.6. Iso-surfaces of $Q = 0.01Q_{\max}$ at $\tau = 700$

Turbulent statistics

In order to compare the DNS results with experimental results of literature the time averaged flow quantities $\langle\bar{\phi}\rangle$ and $\langle\tilde{\phi}\rangle$ are extracted from the flow field during the self-similar time period $(500 < \tau < 800)$. It can be seen from Fig.7 ($\eta = y/\delta_\omega$) that the mean streamwise velocity profiles is in excellent agreement with the incompressible experimental results of [8] and [9].

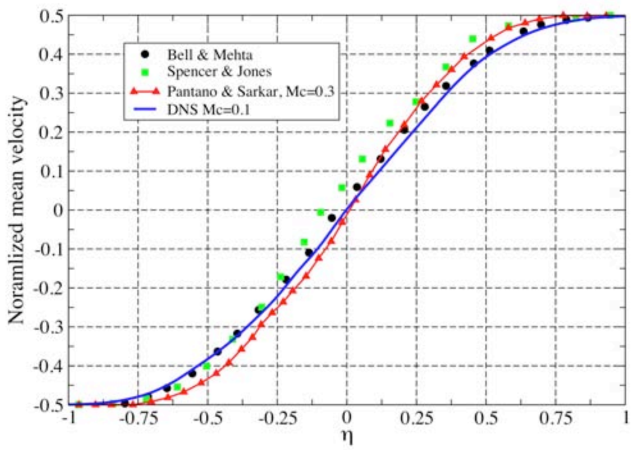

Fig.7. Comparison of mean streamwise velocity $\langle \tilde{u} \rangle / \Delta u$

The turbulent stress tensor R_{ij} is defined by $R_{ij} = \dfrac{\overline{\rho u_i'' u_j''}}{\overline{\rho}}$.

Fig.8 shows the comparison of $\sqrt{\langle R_{ij} \rangle} / \Delta u$ with the experimental and DNS results of literature. Good agreement between the simulated results with the experimental results of [8, 9] as well as with the DNS results of Pantano & Sarkar (M_c=0.3) [6] and [10] have been achieved. Tab.2 summarizes the comparison of peak turbulent intensities. It is evident that fairly good agreement of the measure of anisotropy has also been achieved by the present DNS study.

The Favre-averaged transport equation of turbulent kinetic energy [11] in conservative form is given by,

$$\frac{\partial \overline{\rho} \kappa}{\partial t} + \frac{\partial \overline{\rho} \tilde{u}_j \kappa}{\partial x_j} = P_\kappa + D_\kappa + T_\kappa + P_w + \Pi \tag{5}$$

where the turbulent production, dissipation, diffusion, pressure work and pressure dilatation terms are

$$\begin{cases} P_\kappa = -\overline{\rho u_i'' u_j''} \dfrac{\partial \tilde{u}_i}{\partial x_j} \\ D_\kappa = -\overline{\tau_{ji} \dfrac{\partial u_i''}{\partial x_j}} \\ T_\kappa = \dfrac{\partial}{\partial x_j} \left[\overline{\tau_{ji} u_i''} - \overline{\rho u_j'' \dfrac{1}{2} u_i'' u_i''} - \overline{p' u_j''} \right] \\ P_w = -\overline{u_i''} \dfrac{\partial \overline{p}}{\partial x_j} \\ \Pi = \overline{p' \dfrac{\partial u_i''}{\partial x_i}} \end{cases}$$

The averaged turbulent budget terms $\langle P_\kappa \rangle$, $\langle D_\kappa \rangle$ and $\langle T_\kappa \rangle$ (neglecting the contribution of $\overline{p' u_j''}$, P_w and Π) are shown in Fig.9 to compare with the DNS results of [6] and [10]. It can be seen that, despite of using different turbulence initialization compared to [6, 10], the balance of the turbulent kinetic energy in self-similar state is found to be comparable for the quasi-incompressible case.

	Bell & Mehta	Pantano & Sarkar	DNS
M_c	0.0	0.3	0.1
$\sqrt{\langle R_{11}\rangle}/\Delta u$	0.18	0.17	0.164
$\sqrt{\langle R_{22}\rangle}/\Delta u$	0.14	0.134	0.125
$\sqrt{\langle R_{12}\rangle}/\Delta u$	0.10	0.103	0.107
$\sqrt{\langle R_{22}\rangle/\langle R_{11}\rangle}$	0.777	0.788	0.762
$\sqrt{\langle R_{12}\rangle/\langle R_{11}\rangle}$	0.555	0.606	0.652

Tab.2. Comparison of peak turbulent intensities

The probability density function (PDF) of a standardized random variable is given by

$$P(\hat{\varsigma}) = P\left(\frac{\varsigma - \mu_1}{\sqrt{\mu_2}}\right) \text{ where } \mu_1 = \int_{-\infty}^{+\infty} \varsigma P(\varsigma) d\varsigma \text{ and } \mu_2 = \int_{-\infty}^{+\infty} (\varsigma - \mu_1)^2 P(\varsigma) d\varsigma$$

The PDFs of the flow field parameters are calculated at mid x-z plane, to analyze the statistical behavior of the turbulence for DNS. Figs.10 and 11 show the standardized PDFs of various parameters. It can be seen that the PDFs of velocity fluctuations (Fig. 10) nearly follow the Gaussian distribution (continuous curve), while the PDFs of velocity gradients and vorticities (Fig. 11) are similar to exponential / double exponential distributions with high kurtosis. Tab.3 summarizes the higher moments of all the PDFs. It can be noticed that the positive values are more frequent (skewness) for ω_z with higher exponential tails. The computed kurtosis for velocity fluctuations is close to 3, which is in accordance with the Gaussian behavior. On the other hand, the PDFs of transverse derivatives of the velocity components are having excess kurtosis ≈3, which are similar to the double exponential distribution behavior.

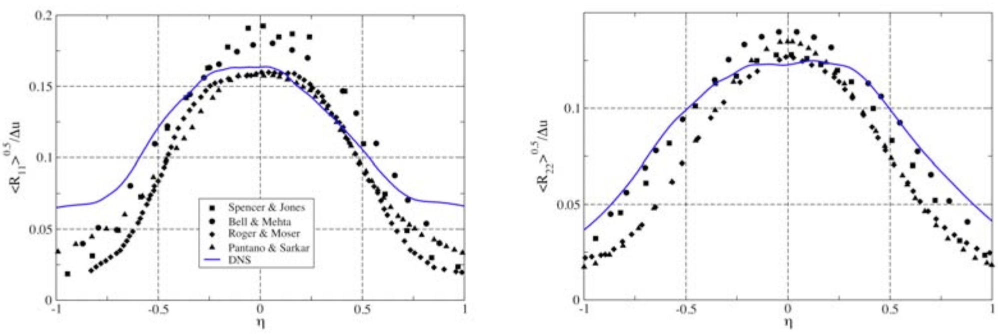

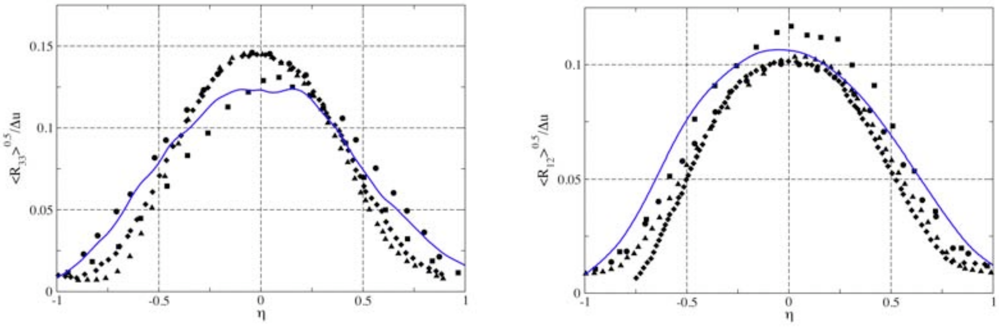

Fig.8. Comparison of turbulent intensities

CONCLUSIONS

An in house 3D compressible multi-species Navier-Stokes parallel solver has been developed utilizing a high-order, low-dissipative optimized shock-capturing WENO-BWO scheme. First, the WENO-BWO scheme with a total variation relative limiter has been used for the prediction of 2D shock/mixing-layer interaction. Then, the DNS study of a temporally evolving mixing layer has been chosen to validate the developed multi-species code in weakly compressible regime. The attainment of the self-similar state and the predicted growth rate are found to be in excellent agreement with the experimental results for incompressible mixing layer. Agreement with the previous experimental and numerical studies of literature has also been successfully achieved through the intense validation of various turbulence quantities. Future studies of spatially evolving supersonic mixing layers (reacting and non-reacting) are the obvious extension of the present work, whose final objective is to investigate the dynamics of mixing-layers and their impact on the nozzle flow separation and the thermal loads under end-effect regimes.

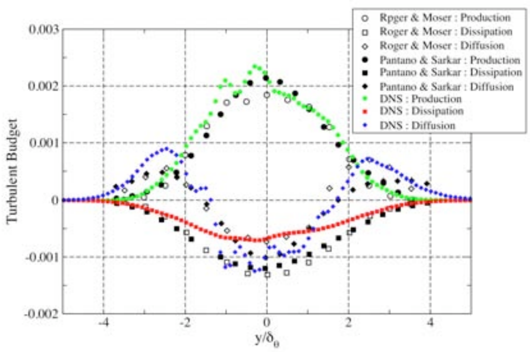

Fig.9. Turbulent budget comparison

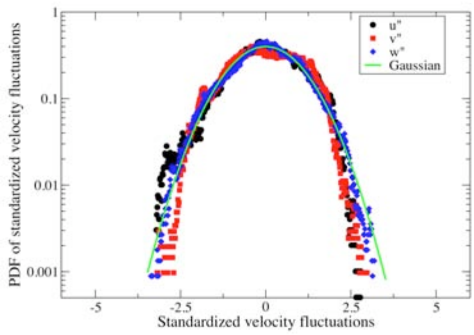

Fig.10. PDFs of velocity fluctuations

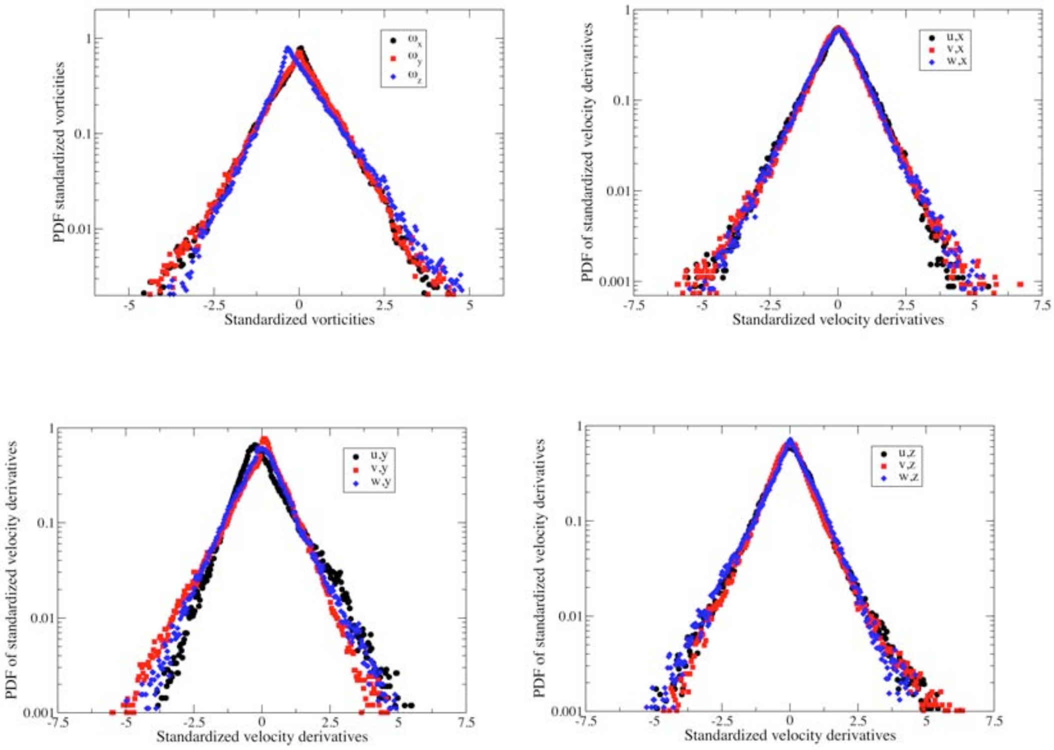

Fig.11 PDFs of vorticities and velocity gradients

Standardized PDF	Skewness	Kurtosis
u''	-0.20	2.91
v''	-0.10	2.37
w''	-0.10	2.88
ω_x	-0.03	9.00
ω_y	-0.04	6.54
ω_z	0.86	7.25
$\partial u/\partial x$	-0.21	5.75
$\partial v/\partial x$	-0.003	7.25
$\partial w/\partial x$	-0.07	6.71
$\partial u/\partial y$	0.93	6.14
$\partial v/\partial y$	-0.54	6.36
$\partial w/\partial y$	0.15	5.98
$\partial u/\partial z$	0.05	6.85
$\partial v/\partial z$	0.31	12.98

$\partial w/\partial z$	-0.34	5.90

Tab.3 Higher moments of PDFs

ACKNOWLEDGEMENTS

The financial support from the CNES (Centre National d'Etudes Spatiales) is gratefully acknowledged. Computational facilities are provided by CINES and IDRIS, France.

REFERENCES

[1] M. P. Martin, E. M. Taylor, M. Wu & V. G. Weirs, A bandwidth-optimized WENO scheme for the effective direct numerical simulation of compressible turbulence, *J. Comp. Phys.*, 220, 270-289, 2006.
[2] GRI-Mech Home Page, http://www.me.berkeley.edu/gri-mech/
[3] G. Jiang and C. W. Shu, Efficient implementation of weighted ENO schemes, *J. Comp. Phys.*,126, 202-228,1996.
[4] A. N. Kudryavtsev and D. V. Khotyanovsky, A numerical method for simulation of unsteady phenomena in high speed shear flows, *In Proc. of* Int. Conf. Methods of Aerophysical Research, 1998.
[5] H. C. Yee, M. Vinokur, and M. J. Djomehri, Entropy Splitting and Numerical Dissipation, *J. Comp. Phys.*, 162, 33-81, 2000.
[6] C . Pantano and S. Sarkar, A study of compressible effects in the high -speed turbulent shear layer using direct simulation, *J. Fluid Mech.*, 451, 329-371, 2002.
[7] M . Klein, A. Sadiki and J. Janicka, A digital filter based generation of inflow data for spatially developing direct numerical or large eddy simulation, *J. Comp. Phys.*,186, 652-665, 2003.
[8] J. H. Bell and R. D. Mehta, Development of a two-stream mixing layer from tripped and untripped boundary layers, *AIAA J.*, 28(12), 2034-2042, 1990.
[9] B. W. Spencer and B. GH. Jones, Statistical investigation of pressure and velocity fields in the turbulent two-stream mixing layer, *AIAA Paper* 71-613, 1971.
[10] M. M. Rogers and R. D. Moser, Direct simulation of a self-similar turbulent mixing layer, *Phys. Fluids*, 6,903-923, 1994.
[11] D. C. Wilcox, Turbulence Modeling for CFD, DCW Industries, Inc., 1993.